3 Data Acquisition and Performance Characterization in PET*

Dale L Bailey

Introduction

Positron emission detection systems have developed since their first use in the 1950s to the high-resolution, high-sensitivity tomographic devices that we have today. Configurations differ far more than for a gamma camera, with such variables as the choice of scintillation crystal, 2D or 3D acquisition mode capability, continuous or discrete detectors, full or partial surrounding of the patient, and a variety of transmission scanning arrangements and radioactive sources. In addition, PET instrumentation is an area that has continued to evolve rapidly, especially over the last decade, with the emphases on increasing sensitivity, improving resolution, and decreasing patient scanning times. This chapter discusses the issues that are determinants of PET system performance. Much of the discussion is based on circular tomographs with discrete detectors, however, the principles are applicable also to flat detector systems and rotating gamma camera PET systems.

Detected Events in Positron Tomography

Event detection in PET relies on electronic collimation. An event is regarded as valid if:

(i) two photons are detected within a predefined electronic time window known as the coincidence window,
(ii) the subsequent line-of-response formed between them is within a valid acceptance angle of the tomograph, and,
(iii) the energy deposited in the crystal by both photons is within the selected energy window.

Such coincident events are often referred to as prompt events (or "prompts").

However, a number of prompt events registered as having met the above criteria are, in fact, unwanted events as one or both of the photons has been scattered or the coincidence is the result of the "accidental" detection of two photons from unrelated positron annihilations (Fig. 3.1). The terminology commonly used to describe the various events in PET detection are:

(i) A *single* event is, as the name suggests, a single photon counted by a detector. A PET scanner typically converts between 1% and 10% of single events into paired coincidence events;
(ii) A *true coincidence* is an event that derives from a single positron–electron annihilation. The two annihilation photons both reach detectors on opposing sides of the tomograph without interacting significantly with the surrounding atoms and are recorded within the coincidence timing window;
(iii) *A random* (or *accidental*) *coincidence* occurs when two nuclei decay at approximately the same time. After annihilation of both positrons, four photons are emitted. Two of these photons from different annihilations are counted within the timing window and are considered to have come from the same positron, while the other two are lost. These events are initially regarded as valid, prompt events, but are spatially uncorrelated with the distribution of tracer. This is clearly a function of the number of disintegrations per second,

---

* Chapter reproduced from Valk PE, Bailey DL, Townsend DW, Maisey MN. Positron Emission Tomography: Basic Science and Clinical Practice. Springer-Verlag London Ltd 2003, 69–90.

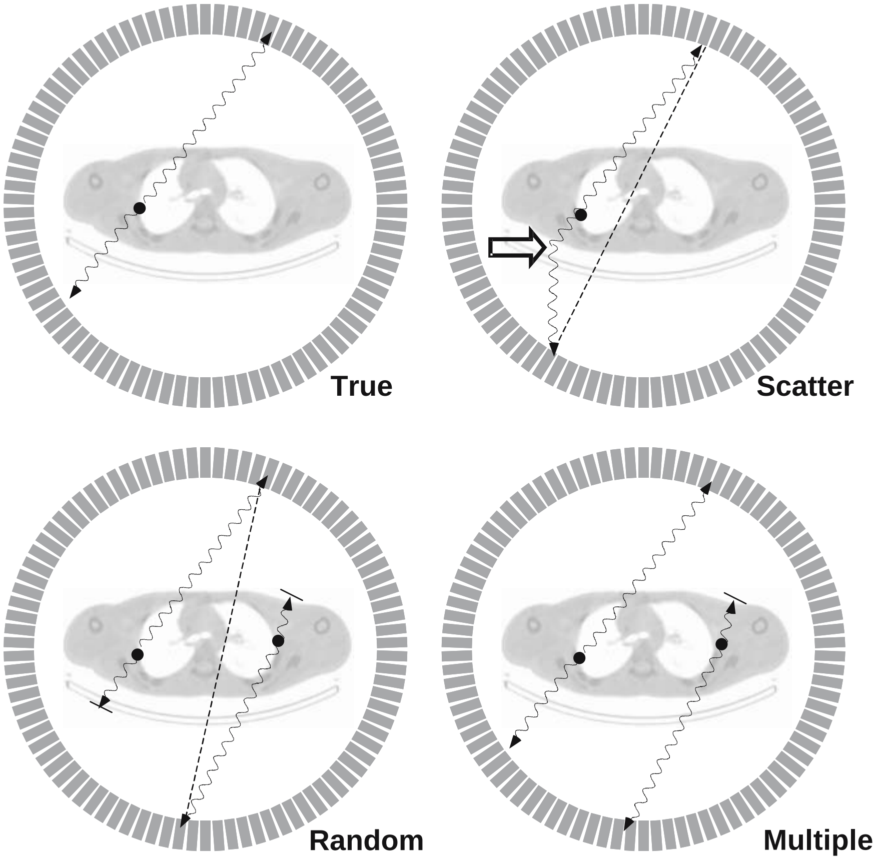

Figure 3.1. The various coincidence events that can be recorded in PET are shown diagrammatically for a full-ring PET system. The black circle indicates the site of positron annihilation. From top left clockwise the events shown are: a true coincidence, a scattered event where one or both of the photons undergo a Compton interaction (indicated by the open arrow), a multiple coincidence arising from two positron annihilations in which three events are counted, and a random or accidental coincidence arising from two positrons in which one of the photons from each positron annihilation is counted. In the case of the scattered event and the random event, the mis-assigned line of response is indicated by the dashed line.

and the random event count rate (R_{ab}) between two detectors *a* and *b* is given by:

$$R_{ab} = 2\tau N_a N_b \qquad (1)$$

where *N* is the single event rate incident upon the detectors *a* and *b*, and 2τ is the coincidence window width. Usually $N_a \approx N_b$ so that the random event rate increases approximately proportionally to N^2. There are two common methods for removing random events: (i) estimating the random event rate from measurements of the single event rates using the above equation, or (ii) employing a delayed coincidence timing window. These methods are discussed in detail in Ch. 6.

(iv) *Multiple* (or triple) *events* are similar to random events, except that three events from two annihilations are detected within the coincidence timing window. Due to the ambiguity in deciding which pair of events arises from the same annihilation, the event is disregarded. Again, multiple event detection rate is a function of count rate;

(v) *Scattered events* arise when one or both of the photons from a single positron annihilation detected within the coincidence timing window have undergone a Compton interaction. Compton scattering causes a loss in energy of the photon and change in direction of the photon. Due to the relatively poor energy resolution of most PET detectors, many photons scattered within the emitting volume cannot be discriminated against on the basis of their loss in energy. The consequence of counting a scattered event is that the line-of-response assigned to the event is uncorrelated with the origin of the annihilation event. This causes inconsistencies in the projection data, and leads to decreased contrast and inaccurate quantification in the final image. This discussion refers primarily to photons scattered within the object containing the radiotracer, however, scattering also arises from radiotracer in the subject but *outside* the coincidence field of view of the detector, as well as scattering off other objects such as the gantry of the tomograph, the lead shields in place at either end of the camera to shield the detectors from the rest of the body, the floor and walls in the room, the septa, and also within the detector. The fraction of scattered events is not a function of count rate, but is constant for a particular object and radioactivity distribution.

The *prompt* count rate is given by the sum of the true plus random plus scattered event rates, as all of these events have satisfied the pulse height energy criteria for further processing. The corrections employed for random and scattered events are discussed in Ch. 6.

The sensitivity of a tomograph is determined by a combination of the radius of the detector ring, the axial length of the active volume for acquisition, the total axial length of the tomograph, the stopping power of the scintillation detector elements, packing fraction of detectors, and other operator-dependent settings (e.g., energy window). However, in general terms the overall sensitivity for true (T), scattered (S), and random (R) events are given by [1–3]:

$$
\begin{aligned}
T &\propto \frac{Z^2}{D} \\
S &\propto \frac{Z^3}{L \times D} \qquad (2) \\
R &\propto \left(\frac{Z^2}{L}\right)^2
\end{aligned}
$$

where Z is the axial length of the acquisition volume, D is the radius of the ring, and L is the length of the septa. For a multi-ring tomograph in 2D each plane needs to be considered individually and the overall sensitivity is given by the sum of the individual planes.

Image Formation in PET

Historically, PET systems have generally developed as circular “rings”. The earliest tomographs consisted of few detectors that rotated and translated to obtain a complete set of projection data, but soon full ring systems were developed. As PET uses coincidence detection, the detectors have to encompass 360° for complete sampling, unlike SPECT (single photon emission computed tomography) where 180° is sufficient. Today, PET systems use either full ring circular (or partial ring) configurations or multiple flat detector arrangements. In the case of gamma camera PET (GC-PET) systems, two or three large-area flat detectors that rotate are employed. Various configurations for PET detector systems are shown in Fig. 3.2.

Radial Sampling

The geometry and coordinate system that will be used to describe the PET systems in this section are shown in Fig. 3.3. The angle that the transaxial (x–y) plane makes with the z-axis is referred to as the polar angle, θ, and the rotated x–y plane forms an azimuthal angle, ϕ, around the object. In 2D PET, data are acquired for $\theta \approx 0°$, while in 3D PET, the polar angle can be opened

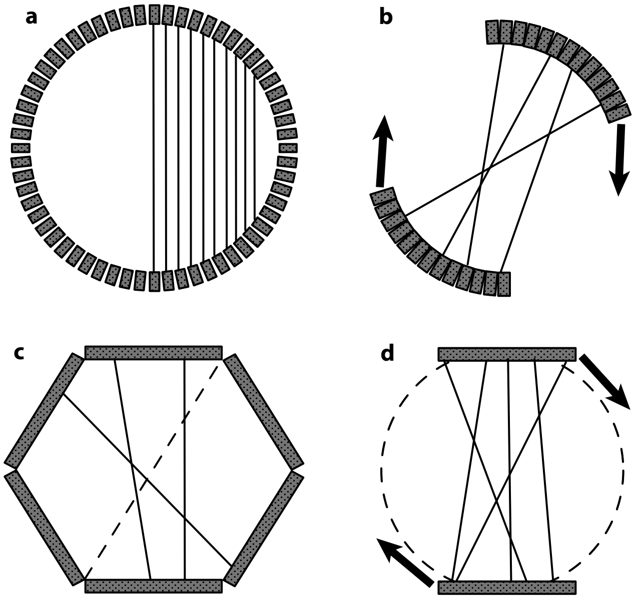

Figure 3.2. Various configurations of PET tomographs are shown in this figure. The solid lines show coincidence lines-of-response (LORs). Configurations (a) and (c) are stationary fixed systems, while (b) and (d) both need to rotate to acquire a complete data set. Configuration (a) is a full-ring circular system, (b) is a partial-ring circular system with continuous rotation, (c) consists of a number (typically 6–8) of flat detectors (LORs not measured indicated by the dashed line), and (d) is the geometry used for gamma camera PET and some other prototype systems using multi-wire proportional counters, where the detectors typically exhibit “step-and-shoot” acquisition protocols to obtain a complete data set.

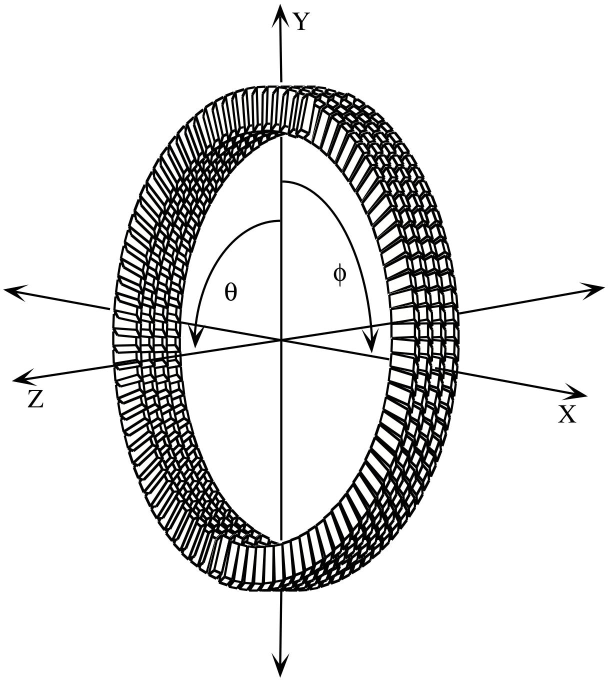

Figure 3.3. A diagram of a full-ring camera is shown with the coordinate system that describes the orientation of the camera. The azimuthal angle (ϕ) is measured around the ring, while the polar angle (θ) measures the angle between rings.

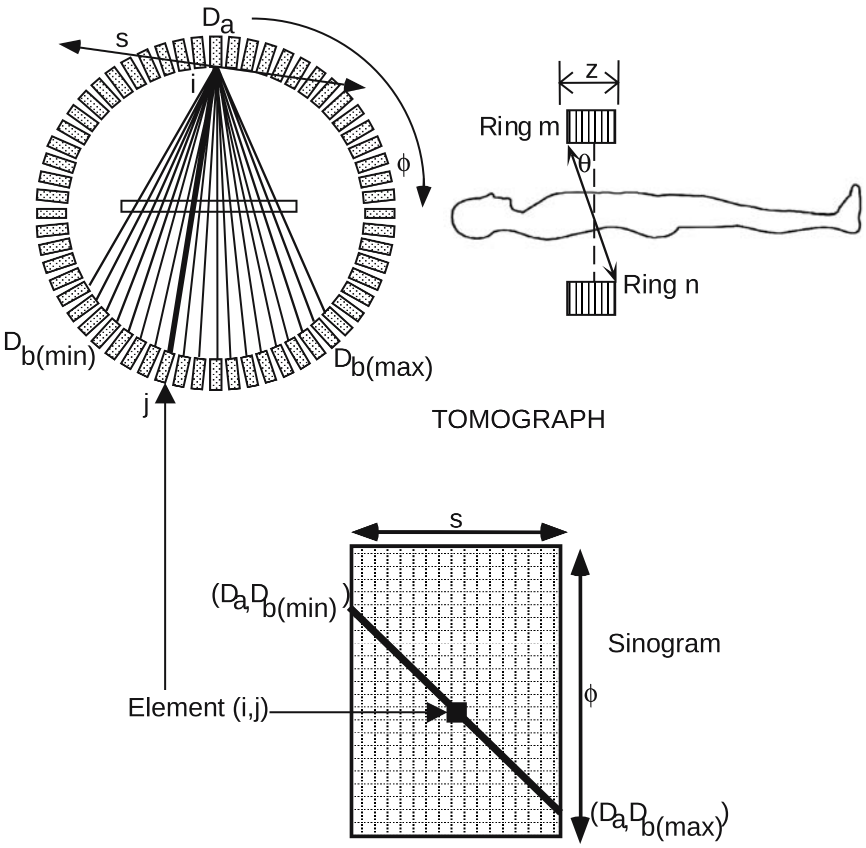

Figure 3.4. The mapping from sampling projections to sinograms is shown. The fan angle of acceptance in the ring in the top left corner maps to a diagonal line in the sinogram.

up to the desired acceptance to strike a trade-off between sensitivity gain and scatter increase.

Individual detector elements form coincidence pairs with opposing detectors (both in-plane and axially) and are mapped to the sinogram space as indicated in Fig. 3.4. Sinograms consist of approximately parallel projections; they are approximately parallel because increased sampling can be achieved by interpolation to form quasi-parallel projections between the detectors that contribute the truly parallel lines of response.

Instead of forming projections between detectors thus:

$$(D_a : D_b), (D_{a+1} : D_{b+1}), (D_{a+2} : D_{b+2}) \tag{3}$$

etc., in effect "double sampling" is achieved with the scheme:

$$(D_a : D_b), (\mathit{D_{a+1} : D}), (D_{a+1} : D_{b+1}), (\mathit{D_{a+2} : D_{b+1}}), (D_{a+2} : D_{b+2}) \tag{4}$$

etc., where the detector combinations in italics are formed between detectors with an offset of one detector between them, but assumed to be parallel to the adjacent projection formed between directly opposed detectors (Fig. 3.5).

The transaxial field of view of a PET tomograph is defined by the acceptance angle in the plane. This is de-

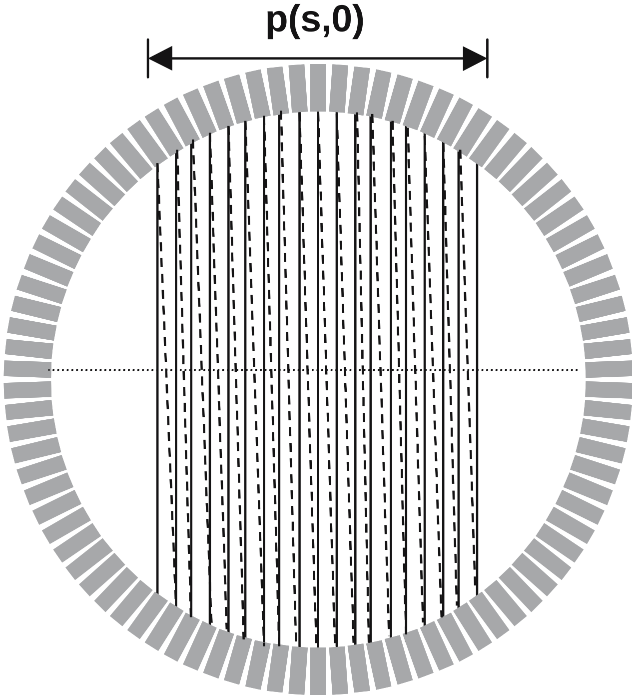

Figure 3.5. Sampling of the projections is doubled by forming coincidences between "opposite-but-one" detectors (dashed lines) as well as with the directly opposed detectors (solid lines). The azimuthal angle assumed for these interpolated lines of response is the same as for the direct lines-of-response. This effectively doubles the sampling in the projections.

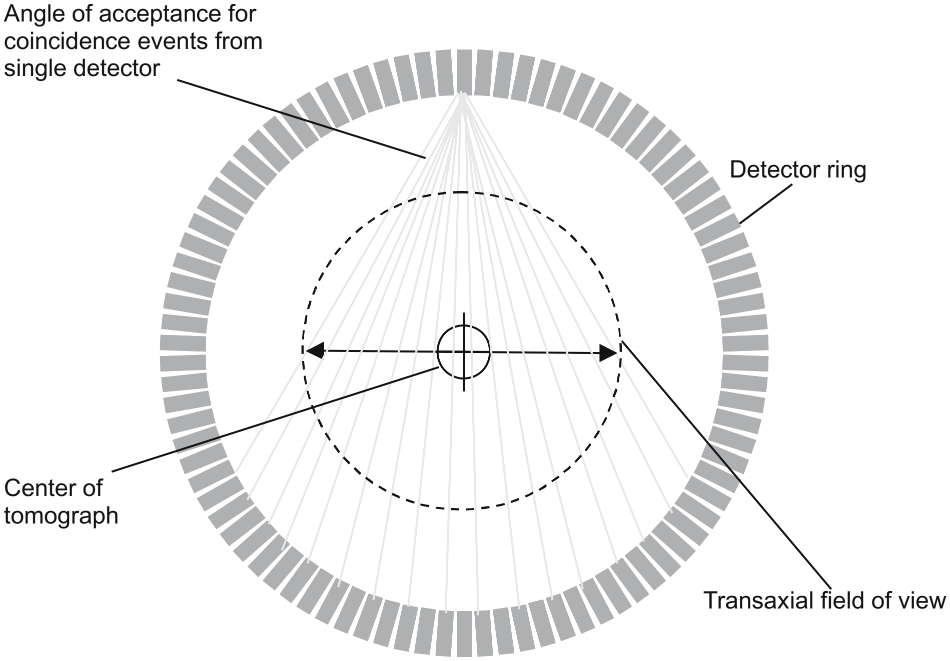

Figure 3.6. The transverse field of view of a PET tomograph is determined by the length of the chord defined by the acceptance angle of the electronics along the central axis of the system.

termined by the electronics, which permit an individual detector to be in coincidence with a finite number of detectors in the opposing side of the ring; the greater the acceptance angle the larger the number of detectors which form the "fan". The width of the fan along the diameter of the tomograph determines the width of the field of view (Fig. 3.6).

The fact that a circular ring is the geometry often used leads to a number of distortions in the sampling which require correction prior to (or as part of) the reconstruction process. The two main effects are:

(i) the distance between the opposing detectors decreases towards the edges of the sampling space (maximum distance from the central line of response). This causes an opening of the acceptance angle and effectively makes these lines of response more sensitive. However, this is offset to some extent by the decreasing surface area of the face of the detector exposed at this increasingly oblique angle, and,

(ii) the lines of response are not evenly spaced in the projection; they get closer together for the lines of response farthest from the central axis of the scanner (see Fig. 3.2(a)). This has the effect of decreasing the inter-detector spacing. Corrections for both effects are discussed in the following chapters.

Axial Sampling

The sinograms formed in PET are composed of projections p (s, ϕ, θ, z). In the 2D case all data are sampled (or assumed to be sampled) with polar angle $\theta = 0°$. In the 3D case this is extended to measuring projections at polar angles $\theta > 0°$. According to Orlov's criteria, the data acquired in 2D are sufficient for reconstructing the entire volume [4, 5]. However, in the 3D case all projections formed from angles with $\theta \neq 0°$ are redundant, as the object can be completely described by the 2D projections. The $\theta \neq 0°$ data are useful, however, as they contribute an increase in *sensitivity* and hence improve the signal-to-noise ratio of the reconstructed data. The redundancy of the oblique lines of response was exploited in the 3D reprojection algorithm [6, 7]. This is discussed further in the next chapter.

A convenient graphical representation was introduced by the Belgian scientist Christian Michel to illustrate the plane definitions used in a large multi-ring PET system, showing how the planes can be combined to optimize storage space and data-handling requirements. They have become known as "Michelogram" representations. Different modes of acquisition are shown in the Michelograms in Fig. 3.7 for a simple eight-ring tomograph.

The situation gets far more complicated for a larger number of rings, and when operating in 3D mode.

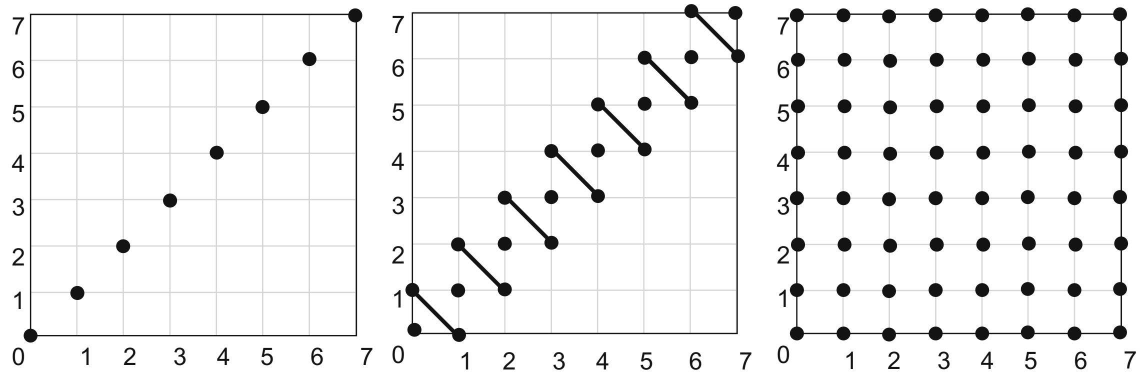

Figure 3.7. The graphical Michelogam is shown for three different acquisition modes on a simple eight-ring tomograph. Each point in the graph represents a plane of response defined between two sets of opposed detectors (a sinogram). In the graph on the left (a simple 2D acquisition with no "inter-planes"), the first plane defined is ring 0 in coincidence with the opposing detectors in the same ring, 0; ring 1 in coincidence with ring 1; etc, for all rings, resulting in a total of eight sinograms. In the middle graph, the same planes are acquired with the addition of a set of "inter-planes" formed between the rings with a ring difference of ±1 ring (ring 0 with ring 1, ring 1 with ring 0, etc). These planes are added together to form a single plane, indicated by the line joining them. This would lead to approximately twice the count rate in this plane compared with the adjacent plane which contains data from one ring only. Physically, this plane is positioned half way between detector rings 0 and 1. While the data come from adjacent rings they are assumed to be acquired with a polar angle of 0° for the purposes of reconstruction. This pattern is repeated for the rest of the rings. This results in 15 (i.e., 2N – 1) sinograms. This is a conventional 2D acquisition mode, resulting in almost twice the number of planes as the previous mode, improving axial sampling, and contributing over 2.5 times as many acquired events. In the graph on the right, a fully 3D acquisition is shown with each plane of data being stored separately (64 in total). The 3D mode would require a fully 3D reconstruction or some treatment of the data, such as a rebinning algorithm, to form 2D projections prior to reconstruction (see Ch. 4).

Examples are shown in Fig. 3.8 for the case of a 48-ring scanner in one particular 2D configuration, with planes added up to a maximum ring difference of ± 4 rings, and in a 3D acquisition configuration, where there are 48^2 (= 2,304) possible planes of response, but in this case the maximum acceptance angle between rings in limited to a ring difference of 40, with up to five axial lines of response being combined into a single plane.

The entire motivation for 3D PET is to increase sensitivity. While radionuclide emission imaging techniques in general use minute tracer amounts (usually micrograms or less), the proportion of the available signal detected is still relatively poor. A radiotracer in most cases distributes throughout the body with only a small fraction localizing in the target organ (if one exists), and collimation, attenuation, and scattering preclude many emitted photons from being detected. A conventional PET camera with interplane septa in 2D mode detects around 4,000–5,000 coincidence events per 10^6 (~0.5%) positron emissions with approximately uniform sensitivity over the axial profile, apart from the less sensitive end planes (Fig. 3.9). A gamma

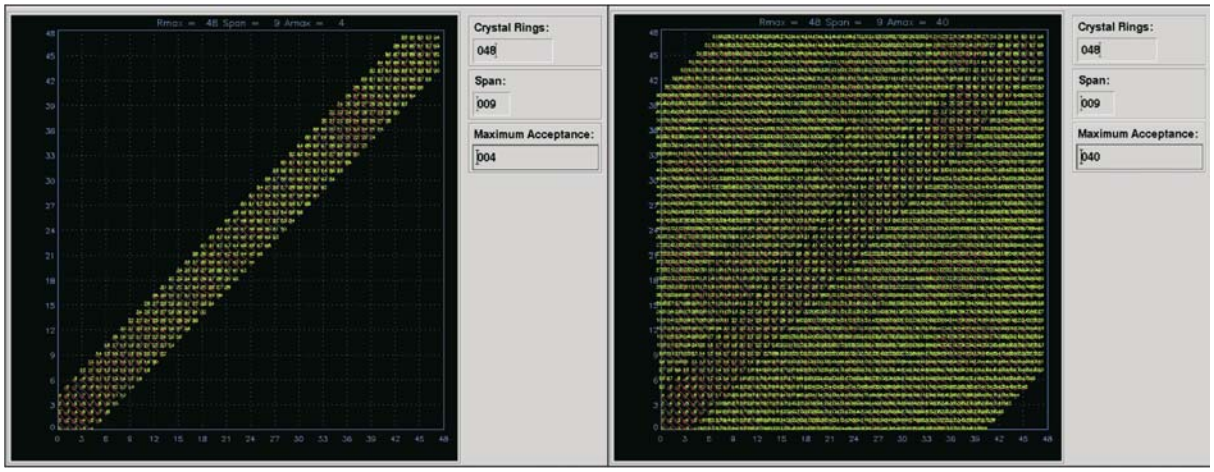

Crystal Rings: 048
Span: 009
Maximum Acceptance: 004

Crystal Rings: 048
Span: 009
Maximum Acceptance: 040

Figure 3.8. Michelograms representing the plane combinations for a 48-ring scanner are shown for the 2D case (left) and the 3D case (right). The x and y axes represent ring numbers on opposing sides of the scanner. Each point on the graph defines a unique plane of response (e.g., all lines-of-response in ring 1 in combination with ring 2).The diagonal lines joining individual dots indicate that the planes of response are combined (added together) thus losing information about each individual point's polar acquisition angle. This form of combination of data from different planes represents a "lossy" compression scheme.

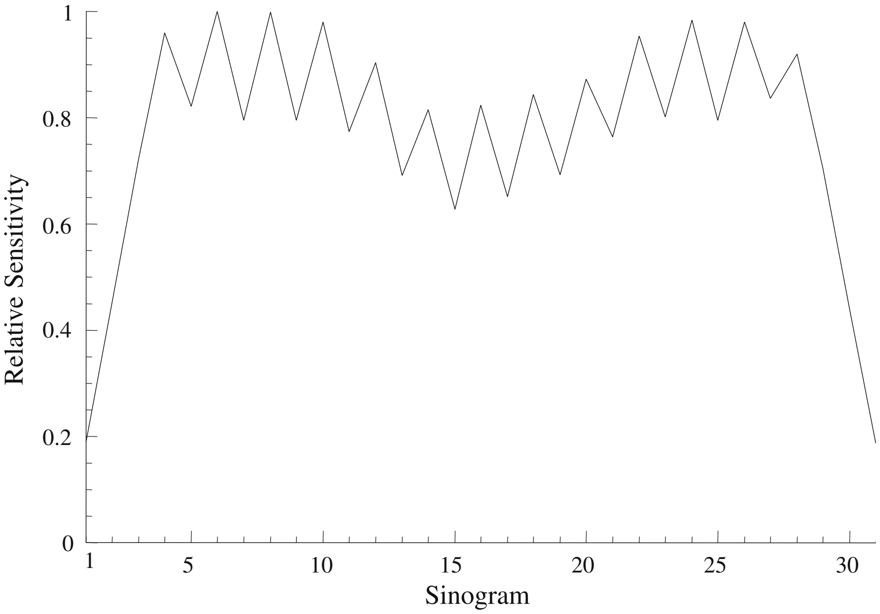

Figure 3.9. The 2D axial sensitivity profile for a line source in air on a 16-ring tomograph (CTI ECAT 951R) demonstrates both the bimodal pattern resulting from the two blocks used in this camera and the sinogram-to-sinogram variation arising from the combination of either three (odd-numbered sinograms) or four (even-numbered sinograms) axial lines-of-response in forming the sinogram. The end sinograms, which contain only one axial line-of-response, are only 20% as efficient as the sinograms formed in the center of the block detector.

camera, with its inefficient lead collimator, detects only around 200 of every 10^6 photons emitted. In spite of this modest efficiency, PET remains the most sensitive emission tomographic modality.

Constraining the allowed coincidences to a narrow plane orthogonal to the z axis of the PET camera severely restricts the overall sensitivity of the technique. Historically, the reasons for this restriction were twofold: the lack of appropriate 3D reconstruction software, and to keep the scatter fraction low. When the interplane septa are removed and all possible lines-of-response within the field-of-view are acquired in 3D, sensitivity is increased by two factors:

(i) the increased number of lines-of-response that it is now possible to acquire without the septa in place, and,
(ii) the amount by which the detector crystals are "shadowed" by the septa when they are in place [7–9]. The 3D acquisition mode leads to a non-uniform axial sensitivity profile, though, as shown in Fig. 3.10 for a 16-ring scanner and a distributed source.

In a 16-ring tomograph the sensitivity gain can be up to around thirty times greater in the center of the scanner compared to the end planes. The "average" gain over the entire axial feld-of-view is around five- to sevenfold. It is possible to separate the contributions of the two factors indicated above by scanning the same source in 2D mode both with and without the interplane septa using the usual 2D configurations of plane-defining lines-of-response. This demonstrates the effect due to septal shadowing alone, seen in Fig. 3.11. The shadowing effect of the septa is greater when the plane definition utilizes cross-planes as is usually done in a conventional 2D acquisition, as would be expected. The average sensitivity improvement due to shadowing is a factor of approximately 2.2. In the studies with a maximum ring difference (d_{max}) of zero, the component of sensitivity lost due to the thickness of the septa themselves (1 mm), and the amount of the detector that this covers is seen in isolation. The second component of the increase in sensitivity is the greater number of lines-of-response that can be accepted in 3D. When the 16 direct rings only are used ($d_{max} = 0$), this corresponds to 16 planes-of-response accepted; with the usual 31 plane definition for 2D acquisitions (ring difference d = 0, ±2 for odd-numbered planes (apart from the end detectors) and d = ±1, ±3 for even-numbered planes) this becomes a total of 100 planes-of-response. In a full 3D acquisition this would become 16 × 16 for this tomograph, i.e., 256 planes-of-response, as now each ring is in coincidence with every other ring on the opposing fan. This gives a factor of 256/100 = 2.56 increase in sensitivity due to the increased numbers of planes accepted compared with conventional 2D mode. However, there is a concomitant increase in the acceptance of scattered events axially as well.

A further effect produces a gain in coincidence count rates in 3D PET compared with 2D in addition to septal shadowing and acquiring more lines-of-response at greater polar acceptance angle. It has been shown that the 3D mode of acquisition is more efficient at converting single events into an annihilation pair which are both detected [9]. Measurements on a first-generation 2D/3D PET system have shown that the conversion rate

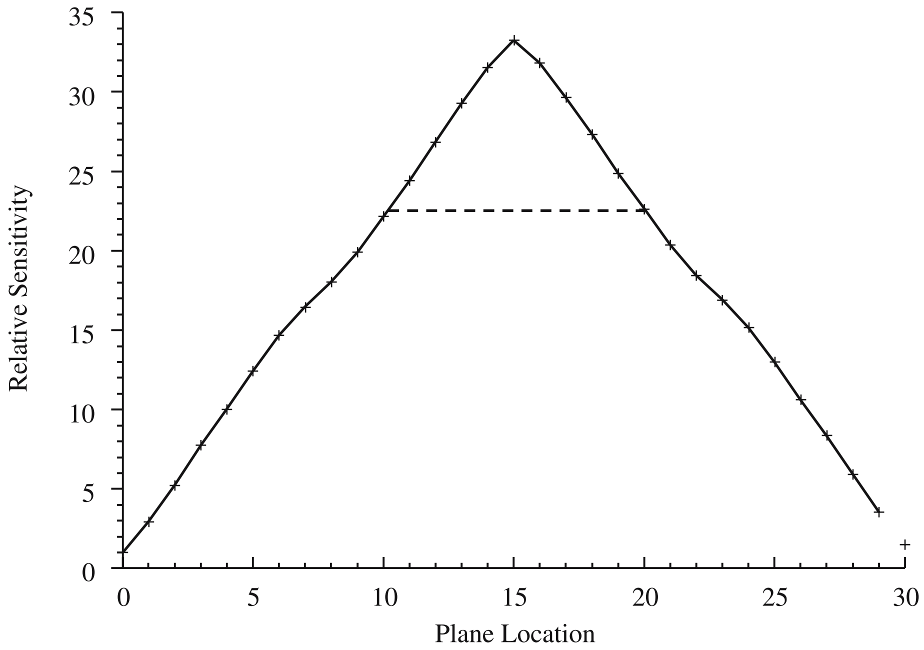

Figure 3.10. The axial sensitivity variation for the 3D acquisition geometry of 16-ring PET camera is shown. The center of the scanner is sampled around 32 times more than the end planes, where all possible planes of response are accepted. The plot is normalized to the first plane. Restricting the maximum acceptance angle (ring difference in this example with discrete detectors) will "flatten" the profile between defined limits (broken line), thereby achieving more uniform sampling in the central axial region of the scanner.

from single events to coincidences for a line source measured in air (i.e., no scatter) was 6.7% in 2D and 10.2% in 3D. For the same source measured in a 20 cm-diameter water-filled cylinder, the conversion rate in 2D was 2.4% and 4.8% in 3D. The ratio of these results show that, without scatter, the increase in conversion from single photons to coincidences for 3D compared to 2D is over 50% (10.2/6.7) higher, and in a scattering medium approaches 100% (4.8/2.4), although many of these events will be scattered events. The explanation is simple: more single photons can now form coincidence pairs in 3D where, in 2D, one or both would have been lost to the system by virtue of the flight angle (outside the allowed maximum ring difference) or by attenuation by the septa.

The non-uniform axial sampling in 3D, however, causes truncation of the projections, which is potentially a far greater problem for reconstruction than an axial variation in sensitivity (Fig. 3.12). This problem was solved, however, in 1989 with the development of the "reprojection" algorithm [6, 7]. This method exploits the fact that the data contains redundancy and the volume can be adequately reconstructed from the direct ring data ($d_{max} = 0$). The first step in this algo-

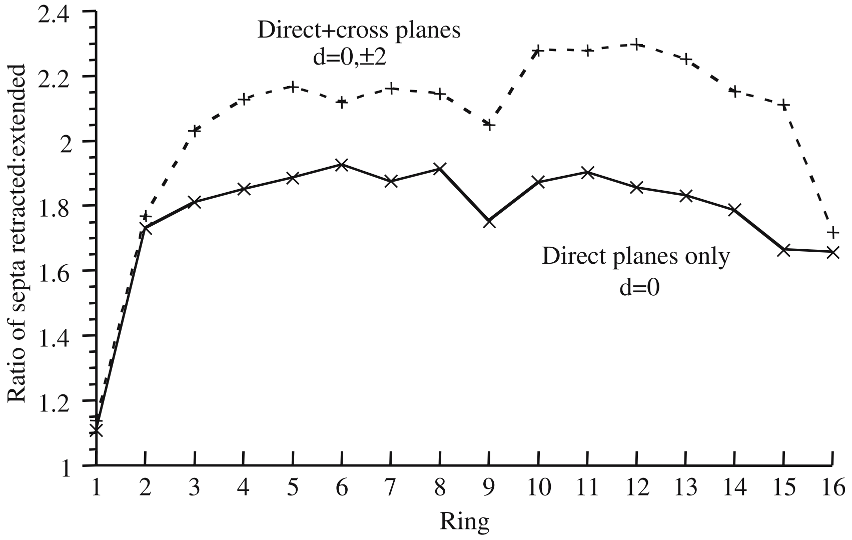

Figure 3.11. Sensitivity improvement due to removal of septa alone is demonstrated. The results are for direct planes only (solid line) and for conventional 2D planes where cross-planes contributions are included (broken line). The "dip" towards the center is at the block boundary of this two-block (axial) tomograph. This shows the effect purely due to septal shadowing.

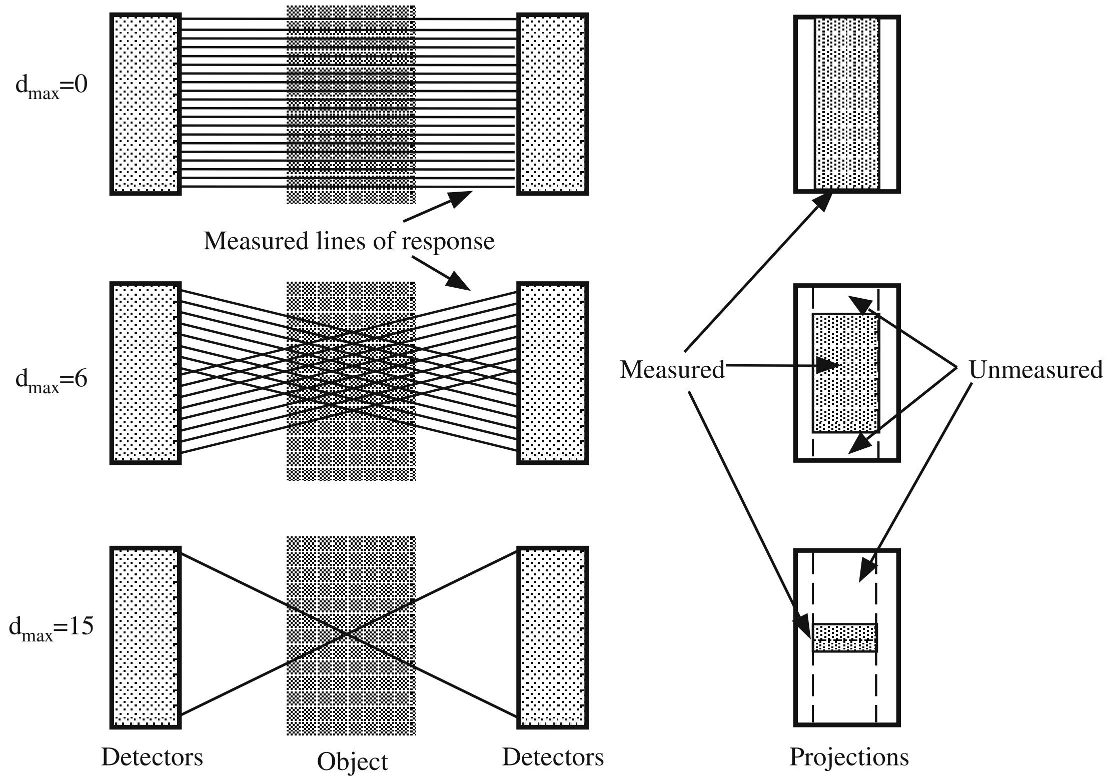

Figure 3.12. In the 3D acquisition case truncation of the projections occurs for those polar angles > 0°. At the top (d = 0) the entire field of view is sampled – this is the usual 2D case. When the ring difference is increased there is truncation of the axial field of view resulting in loss of data corresponding to the ends of the tomograph (center). In the limiting case (bottom) it results in severe truncation of the object.

rithm is to reconstruct the volume from the conventional 2D data sinograms. The unmeasured, or missing, data are then synthesized by forward projection through this volume. After this the data are complete and shift-invariant, and a fully 3D reconstruction algorithm can be used. This algorithm is discussed in depth in the next chapter.

From Projections to Reconstructed Images

Finally in this section, a brief description of how the data discussed are used to reconstruct images in positron tomography is included. The theory of reconstruction is dealt with in detail in the next chapter.

The steps involved and the different data sets required for producing accurate reconstructed images in 2D PET are shown in Fig. 3.13. All data (apart from the reconstructions) are shown as sinograms (i.e., the coordinates are (s,ϕ)). The usual data required are:

(i) the emission scan which is to be reconstructed,
(ii) a set of normalization sinograms (one per plane in 2D) to correct for differential detector efficiencies and geometric effects related to the ring detector, or a series of individual components from which such a normalization can be constructed (see Ch. 6), and,
(iii) a set of sinograms of attenuation correction factors to correct for photon attenuation (self-absorption or scattering) by the object.

The normalization factor singrams can include a global scaling component to account for the plane-to-plane variations seen in Fig. 3.9. The attenuation factor sinograms are derived from a “transmission” scan of the object and a transmission scan without the object in place (often called a “blank” or reference scan); the ratio of blank to transmission gives the attenuation correction factors. The most common method for acquiring the transmission and blank scans is with either a ring or rotating rod(s) of a long-lived positron emitter such as ^{68}Ge/^{68}Ga, with which the object is irradiated [10]. The emission sinograms are first corrected for attenuation and normalized for different crystal efficiencies, and then reconstructed using the filtered back-projection process. During the final step, scalar corrections for dead time and decay may also be applied.

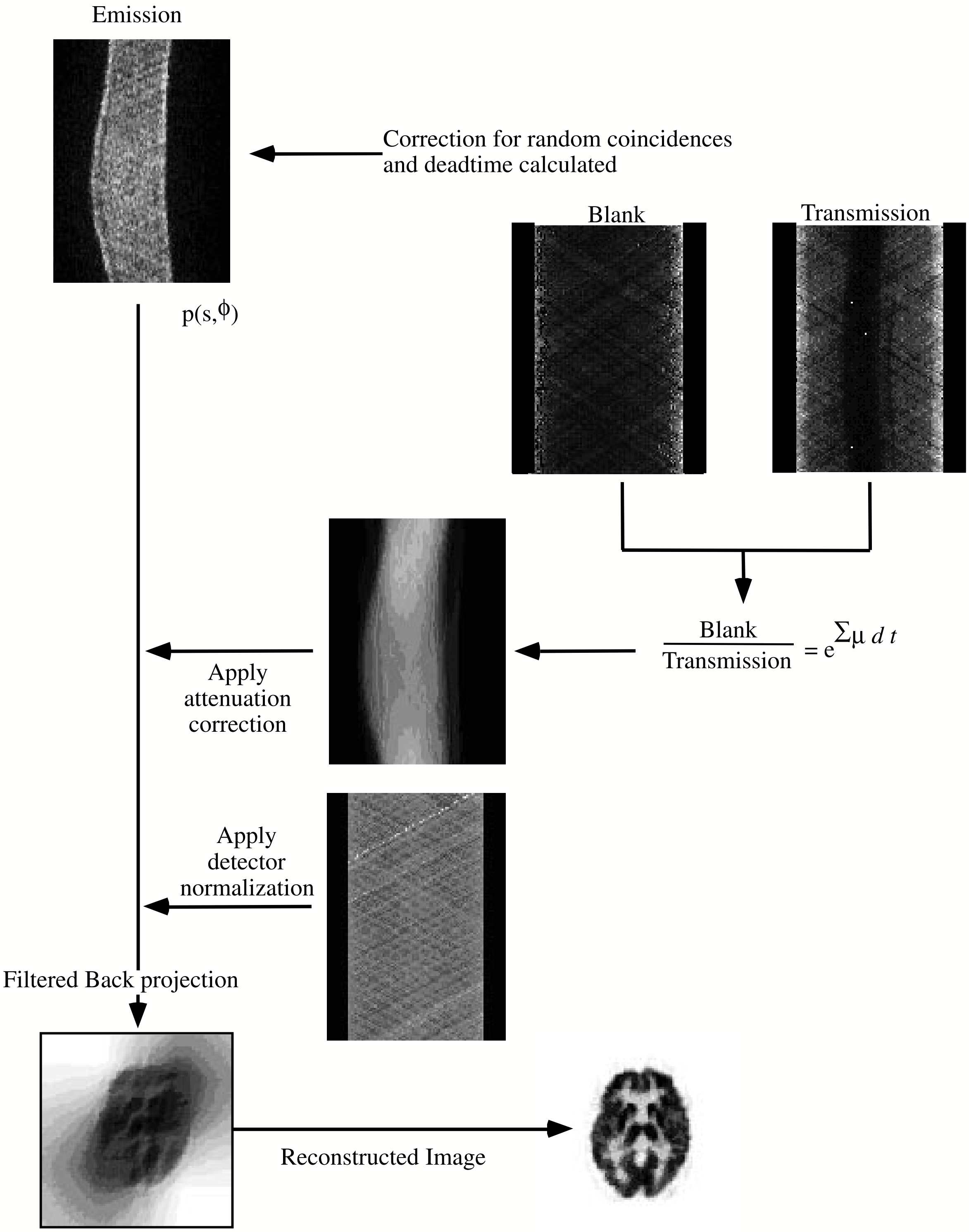

Figure 3.13. The steps involved in producing a 2D PET image are shown using filtered back-projection. Typically 31–95 planes of data are reconstructed in transverse section.

Development of Modern Tomographs

To understand the current state of commercial PET camera design, and why, for example, the development of 3D PET on BGO ring detector systems was only relatively recent, it is instructive to briefly trace the development of full ring PET systems. One of the first widely implemented commercial PET cameras was the Ortec

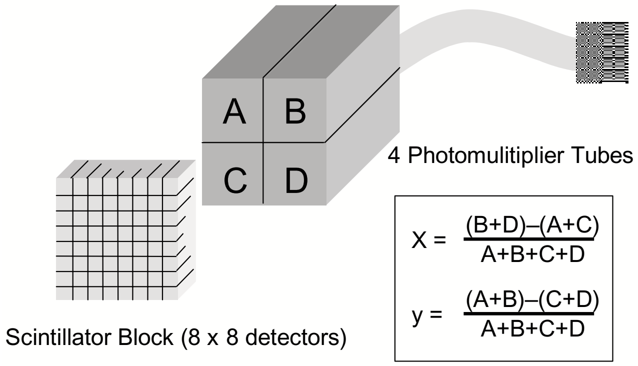

Figure 3.14. A schematic diagram of the block detector system, shown here as an 8 % 8 array of detectors, and the four PMTs which view the light produced is shown. The light shared between the PMTs is used to calculate the *x* and *y* position signals, with the equations shown.

ECAT (EG&G Ortec, Oak Ridge, Tennessee, USA) [11]. This single-slice machine used NaI(Tl) and had a hexagonal arrangement of multiple crystals with rotational and axial motion during a scan. Its axial resolution could be varied by changing the width of the slice-defining lead side shields, thereby altering the exposed detector area. This not only changed the resolution, but also the scatter and random event acceptance rates as well. In their paper of 1979, the developers of this system even demonstrated that in going from their "high-resolution" mode to "low-resolution" mode, they measured a threefold increase in scatter within the object (0.9%–2.7%), although total scatter accepted accounted for only around 15% of the overall signal [12]. In this and other early work on single-slice scanners, the relationship between increasing axial field-of-view and scatter fraction was recognized [1]. Various scintillation detectors have been used in PET since the early NaI(Tl) devices, but bismuth germanate (BGO) has been the crystal of choice for more than a decade now for non time-of-flight machines [13, 14]. BGO has the highest stopping power of any inorganic scintillator found to date.

After the adoption of BGO, the next major development in PET technology was the introduction of the "block" detector [15]. The block detector (shown schematically in Fig. 3.14) consists of a rectangular parallelepiped of scintillator, sectioned by partial saw cuts into discrete detector elements to which a number (usually four) of photomultiplier tubes are attached. An ingenious scheme of varying the depth of the cuts permits each of the four photomultiplier tubes to "see" a differential amount of the light released after a photon has interacted within the block, and from this the point where the photon deposited its energy can be localized to one of the detectors in the array. The aim of this development was to reduce crystal size (thereby improving resolution while still retaining the good-pulse-height-energy spectroscopy offered by a large scintillation detector), modularize detector design, and reduce detector cost. Small individual detectors with one-to-one coupling to photomultiplier tubes is impractical commercially due to packaging limitations and the cost of the large number of components required. The block detector opened the way for large, multi-ring PET camera development at the expense of some multiplexing of the signals. However, a stationary, full ring of small discrete detectors encompassing the subject meant that rapid temporal sequences could be recorded with high resolution, as the gantry no longer needed to rotate to acquire the full set of projections. The evolution and continuously decreasing detector and block size is shown in Fig. 3.15.

The major drawback for the block detector is count-rate performance, as the module can only process a single event from one individual detector in a particu-

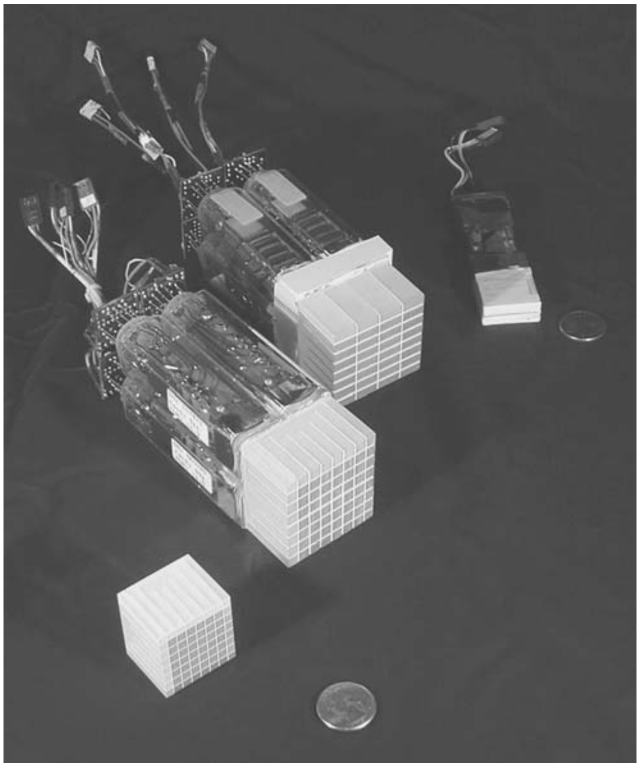

Figure 3.15. The evolution of PET detectors from CTI is shown. In the top right corner is the original ECAT 911 detector, then the first true block detector, the ECAT 93x block (8×4 detectors) with four PMTs attached, the 95x series block, which had double the number of axial saw-cuts, thus doubling the axial sampling compared with the 93x, and the high-resolution ECAT HR+ series block in the bottom left corner, where each detector element measures approximately 4 mm × 4mm × 30 mm. For scale, US25c coins are shown. (Photo courtesy of Dr Ron Nutt, CTI PET Systems).

lar block in a given time interval. Individual detectors with one-to-one coupling to the opto-electronic device would be a lot faster, however, at far greater expense and with a problem of packaging and stability of the great number of devices that would be required.

In a conventional 2D PET camera each effective "ring" in the block is separated by lead or tungsten shields known as septa. The aim was to keep the multi-ring tomograph essentially as a series of separate rings with little cross-talk between rings. This helped keep scatter and random coincidence event rates low, reduce single-photon flux from outside the field of view, and allowed conventional single-slice 2D reconstruction algorithms to be used. However, it limited the sensitivity of the camera.

Alternative systems to block-detector ring-based systems exist. Work commenced in the mid-1970s using large-area, continuous NaI(Tl) flat (or more recently curved) detectors in a hexagonal array around the subject and has resulted in commercially viable systems (GE Quest, ADAC C-PET) [16–19]. These systems have necessarily operated in 3D acquisition mode due to the lower stopping power of NaI(Tl) compared with BGO. The NaI(Tl) detectors, with their improved energy resolution, also provide better energy discrimination for improved scatter rejection based on pulse height spectroscopy. Larger detectors will always be susceptible to dead time problems, however, even when the number of photo-multiplier tubes involved in localizing the event in the crystal is restricted, and hence the optimal counting rates for these systems is lower than one with small, discrete detector elements. This affects clinical protocols by restricting the amount of radiotracer than can be injected.

PET Camera Performance

PET systems exhibit many variations in design. At the most fundamental level, different scintillators are used. The configuration of the system also varies greatly from restricted axial field of view, discrete (block-detector) systems to large, open, 3D designs. With such a range of variables, assessing performance for the purposes of comparing the capabilities of different scanners is a challenging task.

In this section, a number of the determinants of PET performance are discussed. New standards for PET performance have been published which may help to define standard tests to make the comparison of different systems more meaningful [27].

Measuring Performance of PET Systems

Spatial Resolution

Spatial resolution refers to the minimum limit of the system's spatial representation of an object due to the measurement process. It is the limiting distance in distinguishing juxtaposed point sources. Spatial resolution is usually characterized by measuring the width of the profile obtained when an object much smaller than the anticipated resolution of the system (less than half) is imaged. This blurring is referred to as the spread function. Common methods to measure this in emission tomography are to image a point source (giving a *point* spread function (PSF)), or, more usually, a line source (*line* spread function (LSF)) of radioactivity. The resolution is usually expressed as the full width at half maximum (FWHM) of the profile. A Gaussian function is often used as an approximation to this profile. The standard deviation is related to the FWHM by the following relationship:

$$\mathrm{FWHM} = \sqrt{8\log_e 2\sigma} \qquad (5)$$

where σ is the standard deviation of the fitted Gaussian function. There are many factors that influence the resolution in a PET reconstruction. These include:

(i) non-zero positron range after radionuclide decay,
(ii) non-collinearity of the annihilation photons due to residual momentum of the positron,
(iii) distance between the detectors,
(iv) width of the detectors,
(v) stopping power of the scintillation detector,
(vi) incident angle of the photon on the detector,
(vii) the depth of interaction of the photon in the detector,
(viii) number of angular samples, and
(ix) reconstruction parameters (matrix size, windowing of the reconstruction filter, etc.).

Resolution in PET is usually specified separately in transaxial and axial directions, as the sampling is not necessarily the same in some PET systems. In general, ring PET systems are highly oversampled transaxially, while the axial sampling is only sufficient to realize the intrinsic resolution of the detectors. The in-plane oversampling is advantageous because it partially offsets the low photon flux from the center of the emitting object due to attenuation. Transaxial resolution is often subdivided into radial (FWHM_r) and tangential (FWHM_t) components for measurements offset from the central axis of the camera, as these vary in a ring tomograph due to differential detector penetration at different locations in the x–y plane (see Fig. 3.16). Due

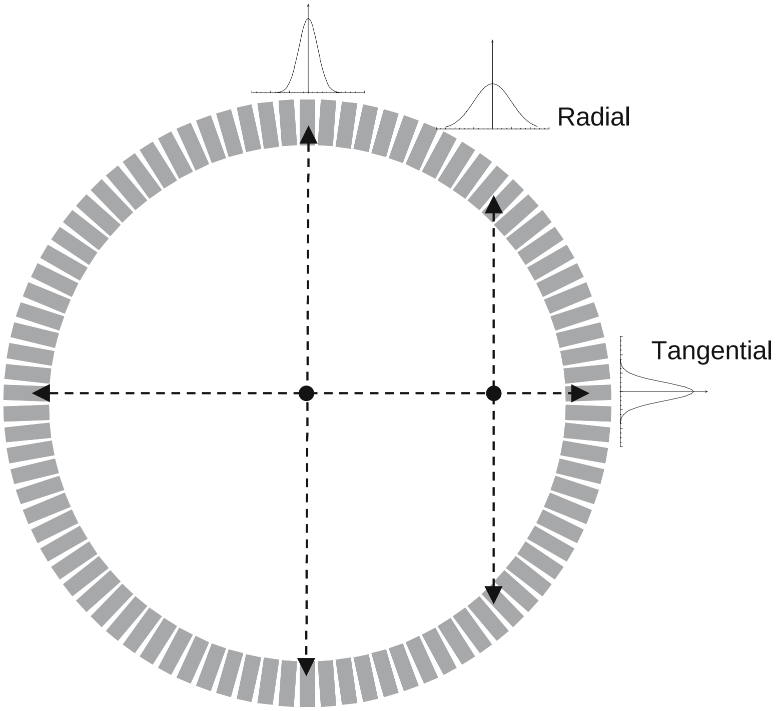

Figure 3.16. Transaxial resolution is separated into tangential and radial components. As the source of radioactivity is moved off-axis there is a greater chance that the energy absorbed in the scintillator will be spread over a number of detector elements. This uncertainty in localizing the photon interaction to one discrete detector degrades the spatial resolution in this direction.

to the limited, discrete sampling in the axial direction with block detector tomographs (one sample per plane), it is inappropriate to measure axial resolution (FWHM_z) on such systems from profiles of reconstructed data as there are insufficient sampling points with which it can be accurately estimated (only one point per plane). However, measurement of axial slice sensitivity of a point source as it passes in small steps through a single slice can be shown to be equivalent to 2D axial resolution, and thus can be utilized to overcome the limited axial sampling to measure the axial resolution.

Energy Resolution

Energy resolution is the precision with which the system can measure the energy of incident photons. For a source of 511 keV photons the ideal system would demonstrate a well-defined peak equivalent to 511 keV. BGO has low light yield (six light photons per keV absorbed) and this introduces statistical uncertainty in determining the exact amount of energy deposited. There are two possible ways to define the energy resolution for a PET scanner: the *single event* energy resolution, or the "*coincidence*" (i.e., both events) energy resolution.

Energy resolution is usually measured by stepping a narrow energy window, or a single lower-level discriminator, in small increments over the energy range of interest while a source is irradiating the detector(s). The count rate in each narrow window is then plotted to give the full spectrum. The data in Fig. 3.17 show the system energy resolution for single photons for a BGO tomograph for three different source geometries. An increase is seen in lower energy events in the scattering medium compared with the scatter-free air measurement.

Energy resolution is a straightforward measurement for single events, but less so for coincidence events. A method often used in coincidence measurements is to step a small window in tandem over the energy range. However, this is not the situation that is encountered in practice as it shows the spectrum when *both* events fall within the narrow energy band. It is more useful is to examine the result when the window for one coincidence of the pair is set to accept a wide range of energies (e.g., 100–850 keV) while the other coincidence channel is narrow and stepped in small increments over the energy range. This allows detection of, for example, a 511 keV event and a 300 keV event as a coincidence (as happens in practice). This is the method used in Fig. 3.18. It demonstrates energy resolution for a line source of ^{68}Ge/^{68}Ga in air of approximately 20% at 511 keV for a BGO scanner, similar to that obtained for the single photon counting spectrum.

Count Rate Performance

Count rate performance refers to the finite time it takes the system to process detected photons. After a photon is detected in the crystal, a series of optical

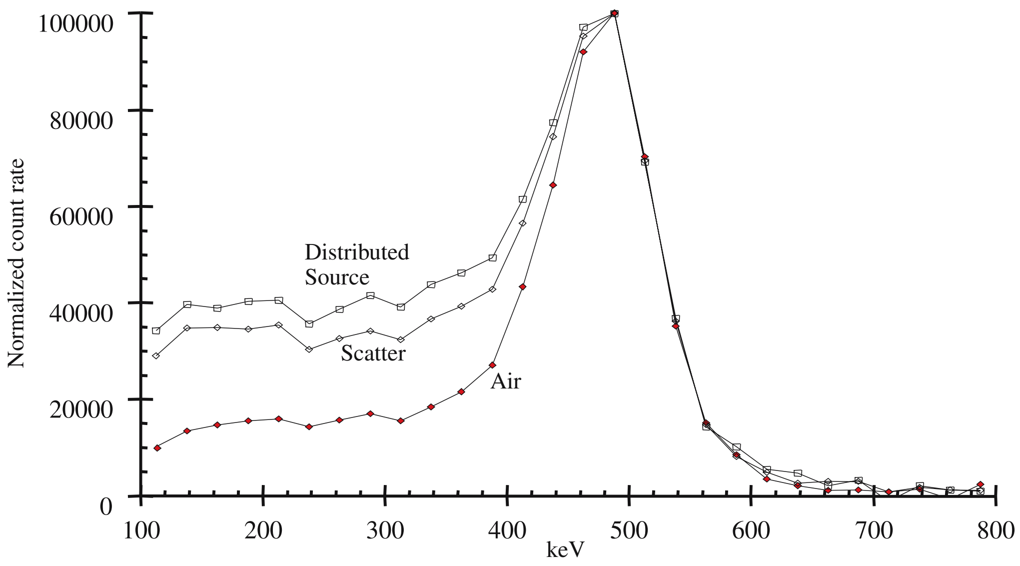

Figure 3.17. The energy spectra for single photons for a BGO PET system. The air and scatter measurements are of a ^{68}Ge line source in air and in a 20 cm-diameter water-filled cylinder respectively, while the distributed source is for a solution of ^{18}F in water in the same cylinder, to demonstrate the effect on energy spectrum of a distribution of activity. The respective energy resolutions are: air – 16.4%, line source in scatter – 19.6%, and distributed source – 21.6%.

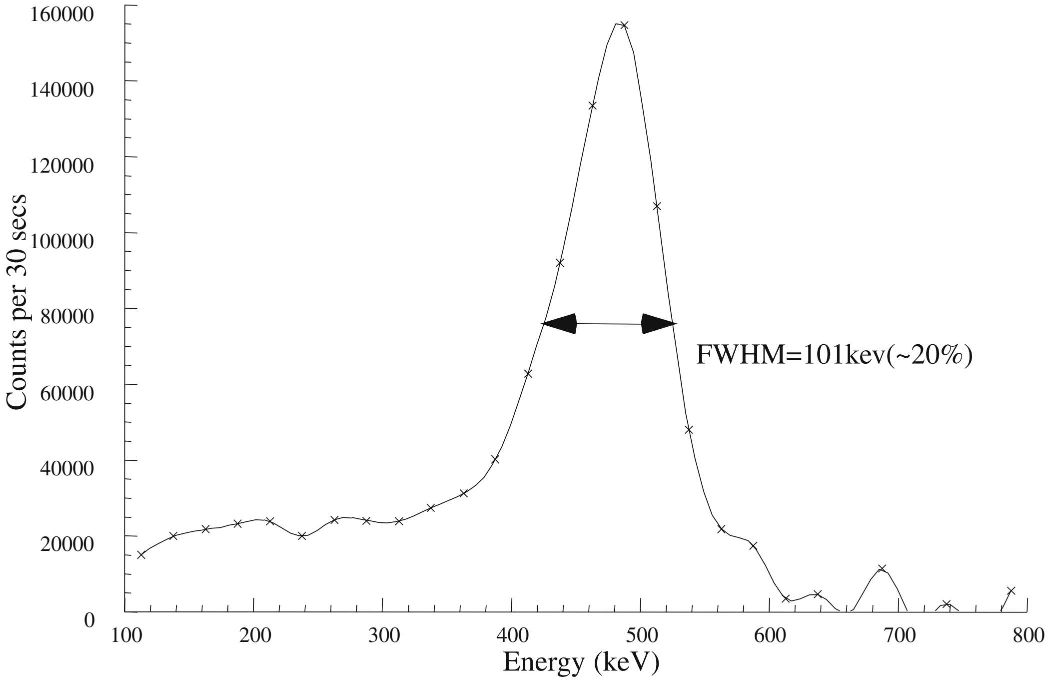

Figure 3.18. The "true" coincidence energy spectrum of a BGO full-ring scanner is shown for a ^{68}Ge line source measured in air. The spectrum is obtained by having one photon energy window set from 100–850 keV and the opposing detector window stepped in small increments of 25 keV to yield an integral coincidence spectrum. The derivative of the integral spectrum results in the above graph.

and electronic processing steps results, each of which requires a finite amount of time. As these combine in series, a slow component in the chain can introduce a significant delay. Correction for counting losses due to dead time are discussed in detail in Ch. 6. In this section we will restrict ourselves to the determination of count rate losses for PET systems for the purposes of comparing performance.

The most common method employed in PET for count rate and dead time determinations is to use a

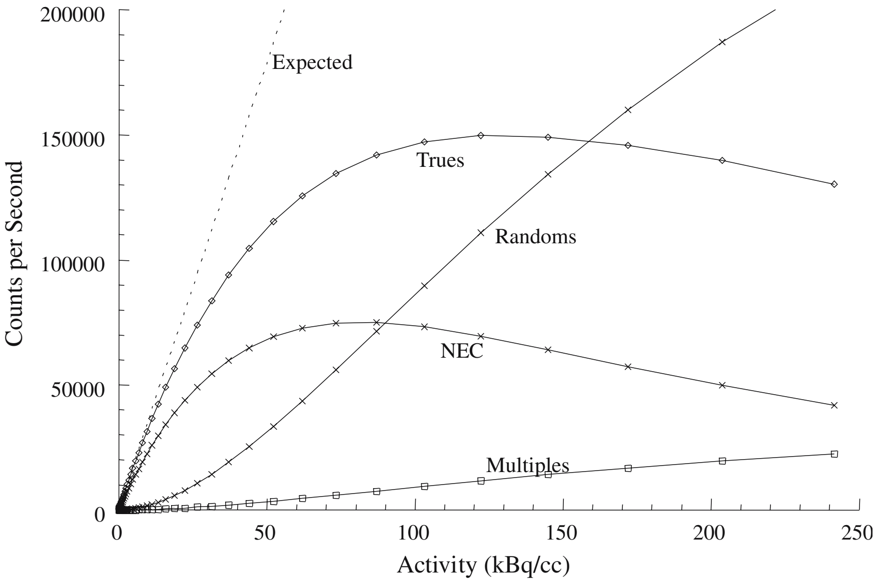

Figure 3.19. Count rate curves are shown for the measured parameters of true (unscattered plus scattered) coincidences, random coincidences, and multiple coincidences (three events within the time window), and the derived curves for expected (no counting losses) and noise equivalent count rate (NEC). The data were recorded on a CTI ECAT 953B PET camera using a 20 cm-diameter water-filled cylinder filled with ^{11}C in water.

source of a relatively short-lived tracer (e.g., ^{18}F, ^{11}C) in a multi-frame dynamic acquisition protocol and record a number of frames of data of suitably short duration over a number of half-lives of the source. Often, a cylinder containing a solution of ^{18}F in water is used. From this, count rates are determined for true, random, and multiple events. The count rates recorded at low activity, where dead time effects and random event rates should approach zero, can then be used to extrapolate an "ideal" response curve with minimal losses (observed = expected count rates). An example of the counting rates achieved for a BGO-based scanner in 2D mode is shown in Fig. 3.19.

It is possible to apply appropriate models to calculate dead time parameters. The data in Fig. 3.19 were characterized by modelling as a cascaded non-paralysable/paralysable system (Fig. 3.20) [20]. From this analysis, the non-paralysable dead-time component (τ_{np}) and the paralysable dead-time component (τ_p) were found to be approximately 3μs and 2μs respectively. Clearly, this is very different to the coincidence timing window duration (in this case $2\tau = 12$ns). The purposes of such parameter determinations might be to derive a dead-time correction factor from the observed counting rates.

The purpose of defining count rate performance is motivated by the desire to assess the impact of increasing count rates on image quality. Much of the theory behind measuring image quality derives from the seminal work of Dainty and Shaw with photographic film [21] and has been applied in a general theory of quality of medical imaging devices to measure detector quantum efficiency [22]. In PET an early suggestion for

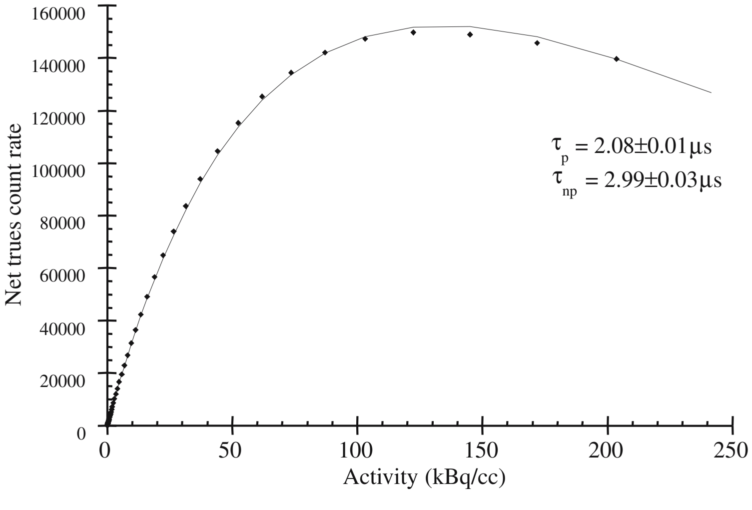

Figure 3.20. The true coincidence count rate for a 16-ring BGO scanner modelled as a combined paralysable and non-paralysable system produces the above fit to the data. From this, estimates of the dead time components can be derived.

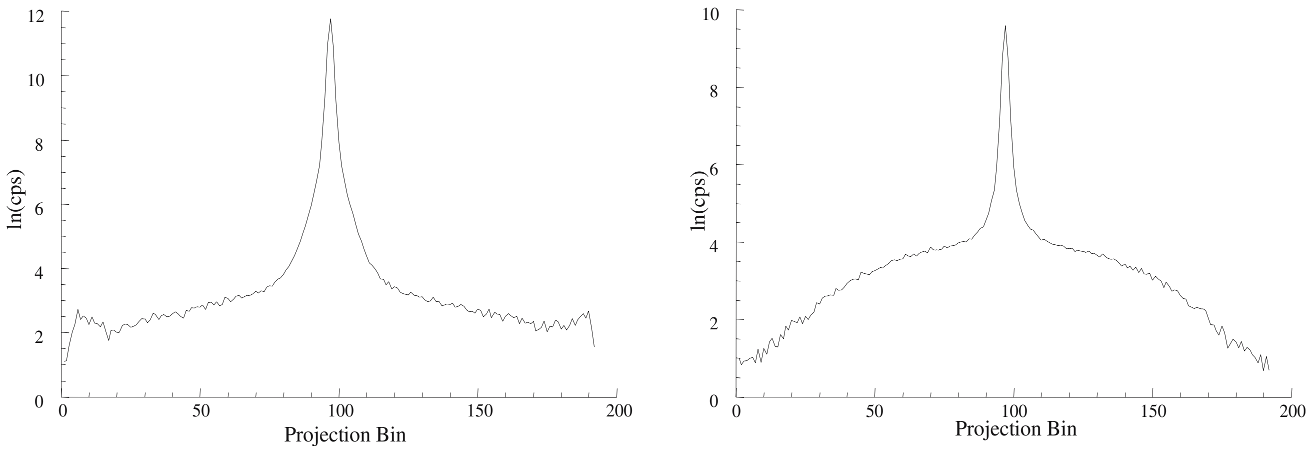

Figure 3.21. Log-linear count rate profiles from sinograms of a line source of ^{68}Ge in air (left) and centered in a 20 cm-diameter water-filled cylinder (right) demonstrate the additive scatter component outside of the central peak in the measurement in the cylinder. Interpolation of this section permits an estimate of the scatter fraction to be made. Both measurements were in 2D mode.

the use of such a figure of merit defined an ‘“effective” image event rate, *Q* to be:

$$Q = D_I \, (d_I \,/\, d_T); \qquad d_T = d_I + d_S + d_A \tag{6}$$

where d_I, d_S, and d_A are the count rates per cm from the center of a uniform cylinder containing radioactivity for the unscattered, scattered, and accidental (random) coincidences respectively, D_I is the total unscattered coincidence rate and (d_I/d_T) is the contrast. It was suggested that “*… Q may also be called an ‘effective’ image event rate, since the same signal-to-noise ratio would be obtained in an ideal tomograph… .*” [2].

This has been further developed in recent years. Comparison of the count rate performance of different tomographs, or of the same scanner operating under different conditions (e.g., 2D and 3D acquisition mode) have been difficult to make because of the vastly different physical components of the measured data (e.g., scatter, randoms) and the strategies for dealing with these. These effects necessitate a comparison which can take account of these differences. The noise equivalent count (NEC) rate [23] provides a means for making meaningful inter-comparisons that incorporate these effects. The noise equivalent count rate is that count rate which would have resulted in the same signal-to-noise ratio in the data in the absence of scatter and random events. It is always less than the observed count rate.

The noise equivalent count rate is defined as:

$$\mathrm{NEC} = \frac{\left[T_{total} \left(\frac{T}{S+T} \right) \right]^2}{(T_{total} + 2fR)} \tag{7}$$

where T_{total} is the observed count rate (including scattered events), *T* and *S* are the unscattered and scattered event rates respectively, *f* is the “random event field fraction”, the ratio of the source diameter to the tomograph’s transaxial field-of-view, and *R* is the random coincidence event rate. This calculation assumes that the random events are being corrected by direct measurement and subtraction from the prompt event rate and that both measurements contain noise, hence the factor of 2 in the denominator (see Ch. 6). The NEC rate is shown, along with the data from which it was derived, in Fig. 3.19.

Some caution is required when comparing NECs from various systems, namely what scatter fraction was used and how it was determined, how the randoms fraction (R) was determined and how randoms subtraction was applied (delay-line method, estimation from single event rates, etc). However, the NEC does provide a parameter which can permit comparisons of count rate, and therefore an index of image quality, between systems.

Scatter Fraction

Scatter fraction is defined as that fraction of the total coincidences recorded in the photopeak window which have been scattered. The scattering may be of either, or both, of the annihilation photons, but it is predominantly scattering of one photon only. Scattering arises from a number of sources:

(i) scattering within the object containing the radionuclide,
(ii) scattering off the gantry components such as lead septa and side shields,
(iii) scattering within the detectors.

A number of methods for measuring scatter have been utilized. Perhaps the simplest method is to acquire data

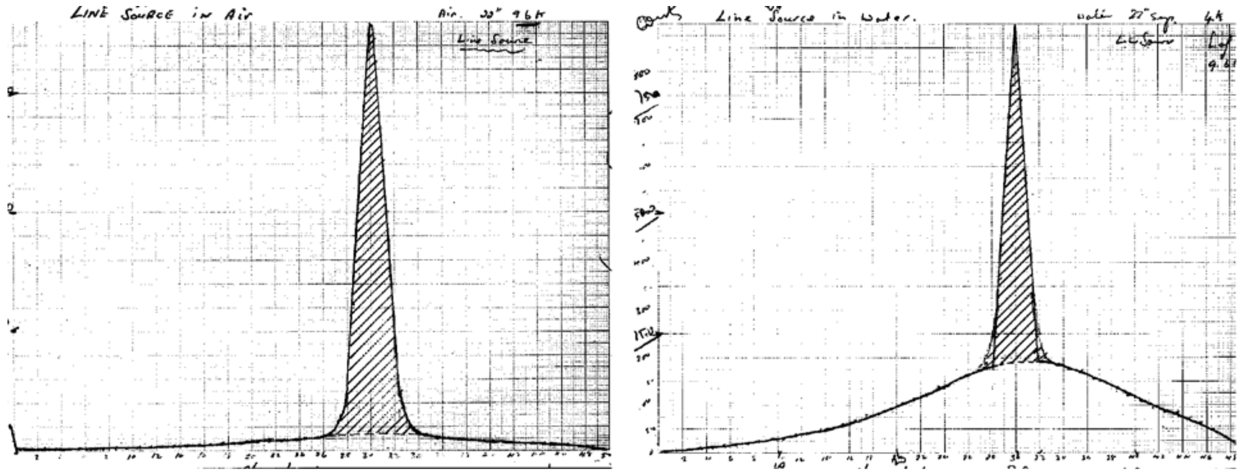

Figure 3.22. One of the earliest demonstrations of scattered radiation in coincidence PET measurements was by Jones and Burnham in 1973 on the first tomographic positron system, the PC-1, developed at the Massachusetts General Hospital in Boston. The process involved measuring a line source suspended vertically in air (left) and then immersing the source in a bucket of water (right) and repeating the measurement. The plots shown here are from the personal notebook of Terry Jones and are reproduced with his permission.

from a line source containing a suitably long-lived tracer in a scattering medium (typically a 20 cm-diameter water-filled cylinder) and produce profiles in the *s* dimension. Interpolation under the peak of the profile recorded outside the known location of the source permits an estimate of the scatter contribution, as used in the previous standard defined by the National Electrical Manufacturers' Association (NEMA) [24]. One criticism of this approach, however, is the assumption about the shape of the "wings" extending into the central section of the profile under the peak, and whether or not it be included in the scatter or non-scattered term (Fig. 3.21).

Scatter in 2D PET is usually relatively small and typically less than 15% of the total photopeak events. Thus it has been a small correction in the final image and often ignored with little impact on quantitative accuracy. The first scatter correction régimes for emission tomography were in fact developed for 2D PET [25].

The largest single difference between 2D and 3D PET after the increase in sensitivity is the greatly increased scatter that is included in the 3D measurements. Septa were originally included in PET camera designs for two reasons: (i) 3D reconstruction algorithms did not exist at the time, and (ii) to restrict random, scattered, and out of field-of-view events. One of the earliest demonstrations of scattered radiation in an open PET geometry was measured on the first positron tomograph PC-1 [26] in Boston in November 1973 shown in Fig. 3.22. Data were taken on this system which comprised two planar opposed arrays of NaI(Tl) detectors. This demonstrates clearly the increase in scatter in the profiles.

Scatter constitutes 20–50%+ of the measured signal in 3D PET. The scatter is dependent on object size, density, acceptance angle, energy discriminator settings, radiopharmaceutical distribution, and the method by which it is defined. The scatter fraction and distribution will vary for distributed versus localized sources of activity, and as such, the method for measuring and defining scatter as well as the acquisition parameters (axial acceptance angle, energy thresholds, etc) need to be quoted with the value for the measurement. In the updated NEMA testing procedures [27] a line source of ^{18}F positioned 45 mm radially from the center of a 20 cm diameter by 70 cm long water-filled cylinder is used to measure the scatter fraction. The scatter is measured on the projections by considering the events detected in the region outside of the cylinder boundary +20 mm on each side, which is interpolated to estimate the scattered events within the peak of the line source location. As mentioned in Ch. 2, scatter in PET is not strongly correlated spatially with the object boundary as it is in SPECT as the line of response from two photons is used. This is dramatically demonstrated in Fig. 3.23, which shows diagrams of the profiles of count rate obtained when a line source is moved laterally in a fixed-position water-filled cylinder. Even when the line source is centered within the object, the profile does not show any discontinuity at the boundary of the cylinder.

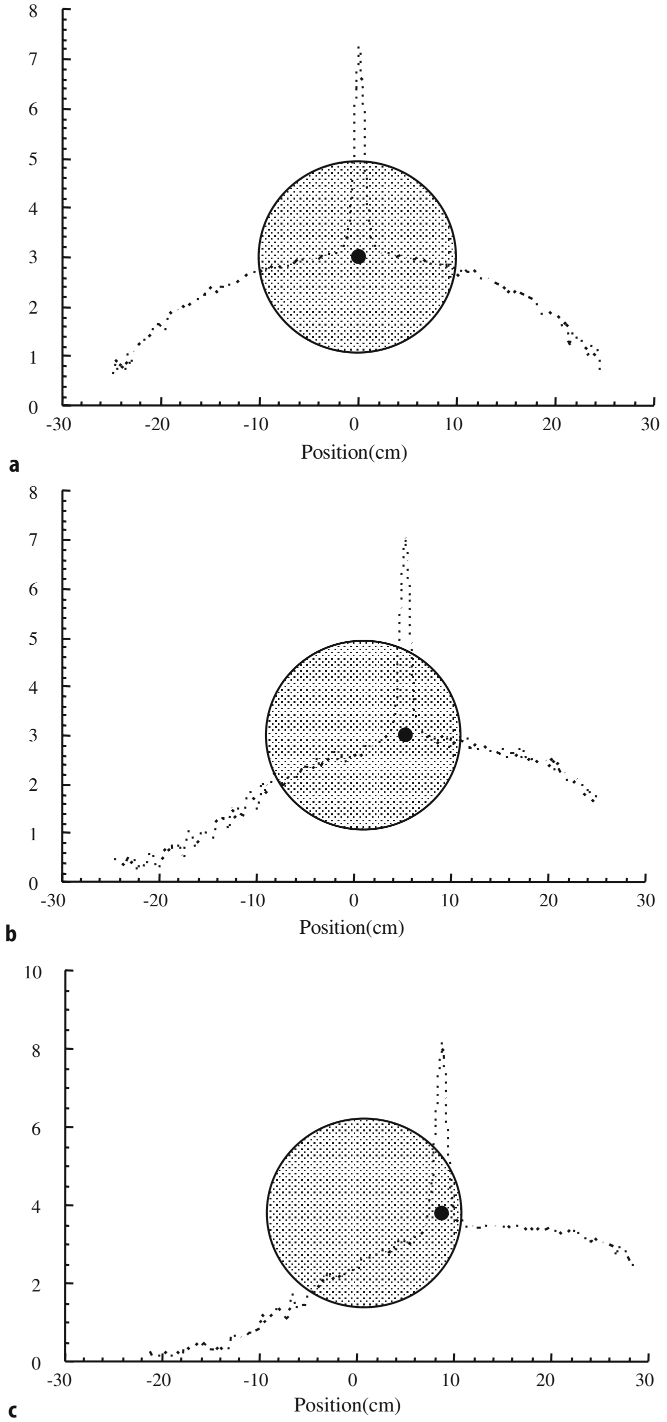

Figure 3.23. Demonstration of the spatial nature of scatter in 3D PET. The graphs show the profile from a line source in a water-filled cylinder in three different positions, with cylinder (grey circle) and line source (black dot) locations superimposed (to scale). The scatter profiles clearly demonstrate that the distribution of the scattered lines of response are only poorly correlated with the object, and can extend a large distance outside of the object. This is not true for SPECT where all scatter is constrained within the object boundaries. The reason for this is that two photons detected are ascribed a line of response joining the detectors in which they deposited their energy, and this can occur well beyond the object boundary.

Chapter 6 covers scatter correction techniques in detail.

Sensitivity of Positron Tomographs

The most commonly used mode for PET scanning at present is the 2D mode, with performance attributes as described in this chapter. Many of the corrections required (such as for dead time and crystal efficiency normalization) are well understood, making quantitative measurements accurate and precise. This has allowed PET to be used routinely as a highly sensitive tool for in vivo functional studies in spite of the 0.5% overall efficiency. However, while the sensitivity of 2D PET is unquestionably high compared with other modalities, the absolute sensitivity remains low compared with the potential signal available from the radiotracer, and consequently there remains room for improvement not only in detection efficiency, but in improving the spatial resolution of the technique as well. As Hoffman has shown, resolution improvements must be accompanied by an approximately third-power increase in sensitivity to maintain equivalent signal-to-noise ratio to realize the improvement in image quality [28]. This is intuitively seen by considering a twofold improvement in resolution: this decreases the effective resolution volume by two in each of the x, y, and z directions and therefore a 2^3 increase in sensitivity would be required to maintain equivalent signal-to-noise ratio per voxel. This is partially offset, though, by an effect known as signal amplification [29], which has guided PET detector designs for over a decade now. Signal amplification essentially means that an improvement in resolution *per se* will lead to an improvement in signal-to-noise in the reconstructed image as the higher resolution means that the reconstructed values will be "spread" over a smaller region, due purely to the higher resolution. This is turn means a higher reconstructed count within the region containing the activity, and hence better noise properties. However, increasing sensitivity still remains the main focus for improving the quality of PET data, and for these reasons the challenge in recent years has focussed on improving sensitivity.

The purpose of a sensitivity measurement on a positron tomograph is primarily to facilitate comparisons between different systems, as, in general, the higher the sensitivity the better signal-to-noise ratio in the reconstructed image (neglecting dead time effects). The sensitivity of positron tomographs has traditionally been measured using a distributed source of a relatively long-lived tracer, such as ^{18}F, in water. The value was quoted in units of counts per second per microCurie per millilitre (cts.sec^{-1}.μCi^{-1}.ml^{-1}) in non-SI units, without correction for attenuation or scattered radiation. This measurement was adequate to compare systems of similar design, e.g., 2D scanners with limited axial field of view. However, with the advent of vastly different designs emerging, and, especially, the use of 3D acquisition methods, this approach is limited for making meaningful comparisons. In 3D, scatter may constitute 20–50% or more of the recorded events and this needs to be allowed for in the sensitivity calculation. In addition, comparison of the true sensitivity compared to SPECT would be meaningless due to the differing attenuation at the different photon energies used. Thus, an absolute sensitivity measurement that is not affected by scatter and attenuation is desirable. A simple source of a suitable positron emitter could be used, however, a significant amount of surrounding medium is required for capture of the positrons within the source, which in itself causes attenuation of the annihilation photons.

A method has been developed to make absolute sensitivity measurements in PET [30], and has been adopted in the new updated NEMA testing procedures [27]. It employs the measurement of a known amount of ^{18}F (or ^{99m}Tc for SPECT) in a small source holder made from aluminum. The thickness of the aluminum wall of the source holder used is sufficient to stop all of the positrons, causing annihilation radiation to be produced, but which also causes some attenuation. The count rate for this source is found by measuring it for a defined period in the camera. Next, another tube of aluminum of known thickness is added to the holder, causing further attenuation, and this is counted again. This is done for a number of extra tubes of aluminum, all of known thickness, and an attenuation curve is produced. The extrapolated y-intercept from this curve gives the "sensitivity in air" for the camera. The units of this measurement are ct.sec^{-1}.MBq^{-1}. This provides an absolute measure of sensitivity. The method can also be used for PET system calibration of reconstructed counts without requiring scatter or attenuation correction [31].

In spite of the improvements in sensitivity with 3D PET, however, much of the available signal still goes undetected. Due to scatter, dead time, and random event rates, the *effective sensitivity* is far less than is measurable in an "absolute" sense. In an attempt to quantify this, a parameter combining the NEC with the absolute sensitivity measurements has been proposed [32]. At extremely low count rates where detector dead time and random events are negligible, the effective sensitivity (as it relates to the image variance) in a distributed object is simply the absolute sensitivity level with a correction for the scatter in the measurement. As the count rate increases, this effective sensitivity decreases due to the increased dead time and random events while scatter remains constant. Therefore, the effective sensitivity as a function of count rate can be expressed as the quotient of the noise equivalent rate divided by the ideal trues count rate with no scatter, dead time or random events, multiplied by the absolute sensitivity. The effective sensitivity, $C_{Eff}(a)$, is defined as:

$$C_{Eff}(a) = \frac{NEC\,(a)}{T_{Ideal}\,(a)} \times C_{Abs} \tag{8}$$

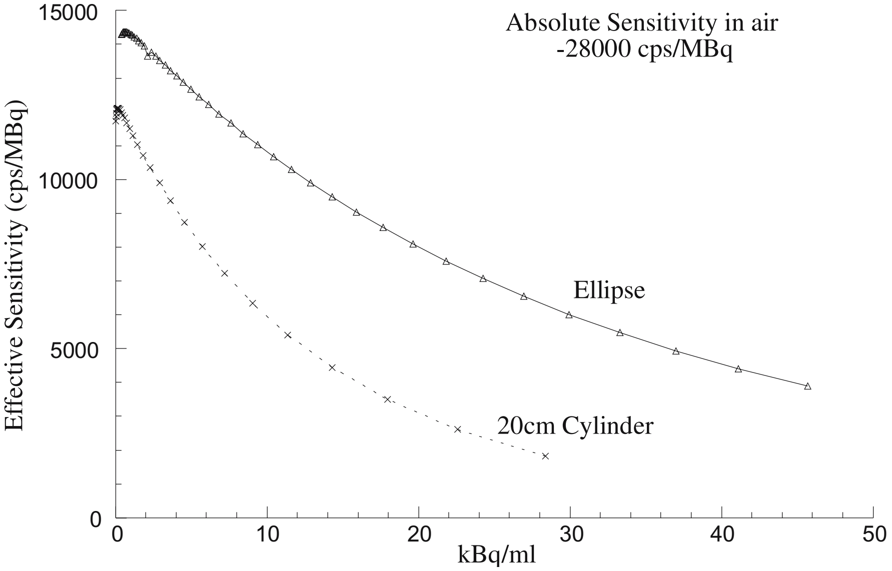

Figure 3.24. Effective sensitivity (cps/MBq) is shown as a function of activity concentration for two different elliptical phantoms (ellipse = 20.5×16.5 cm in cross-section and 20 cm axially approximating an average head size, and a 20 cm-diameter circular cylinder). The system used was a first-generation 2D/3D tomograph (ECAT 953B, CTI) operated in 3D mode. The curves demonstrate the loss of the ability to process events as activity concentration increases.

where C_{Abs} is the absolute sensitivity and $NEC(a)$ and $T_{Ideal}(a)$ are the noise equivalent and ideal (no count rate losses or random events) trues rates, respectively, which are functions of the activity concentration in the object. The effective sensitivity is a function of the activity in the object. This effective sensitivity is shown for 3D measurements using a small elliptical cylinder and a 20 cm cylinder in Fig. 3.24. The effective sensitivity demonstrates that the increase in solid angle from 3D acquisition is only one aspect of improving the sensitivity of PET, and that increasing detector performance by keeping the detectors available for signal detection for a longer proportion of the time can be thought of in a similar manner to increasing the solid angle as both improve the sensitivity of the device.

Other Performance Measures

In addition to the parameters described above (resolution, count rate, scatter, sensitivity), a number of other parameters are specified by bodies such as NEMA to assess PET scanner performance. These include accuracy of corrections for attenuation, scatter, randoms and dead time, and image quality assessments. Uniformity is another parameter that has been found to be useful to test. Energy resolution, though a major determinant of PET performance, has not been included in the latest NEMA PET tests [27]. No explicit tests for assessing transmission scan quality are specified, although a need exists with the variety of systems now available.

A difficulty in extrapolating from performance in standards test to the clinical situation is the highly unrealistic (clinically relevant) nature of the objects scanned. This has been recognized and attempts to address this have been made by employing long test objects (70 cm cylinder, NEMA) and objects which resemble the body in cross-section (EEC phantom [33]).

Impact of Radioactivity Outside the Field of View

Scanner design has traditionally included significant lead end-shields to restrict the majority of single photons emitted from outside the axial field of view of the scanner from having direct line-of-sight trajectories to the detectors. Single photons from outside the field of view will not form a true coincidence, but will increase the number of events the detector has to process leading to increased dead time and random coincidences. Some true coincidences from scattered photons may be included if the positron annihilation was just outside the axial field of view, but in general, the photons from outside the field of view will be unpaired events.

Single photons from outside the field of view were not a large problem with 2D tomographs that used interplane septa, as the septa added extra shielding for the detectors for photons from outside the field of view as well as inside. However, a number of developments over the past decade have exacerbated this situation:

(i) the move to acquire data in high-sensitivity 3D mode, thereby removing the interplane septa,
(ii) the increase in length of the axial field of view, which has the effect of increasing the acceptance angle for single photons from outside the field of view, and,
(iii) decreasing the length of the end shielding to accommodate large subjects. This has the effect of "opening up" the acceptance angle even further.

Examples illustrating this effect are shown in Fig. 3.25. It is a particular issue when using detectors such as BGO or NaI(Tl), which are not fast scintillators, and coincidence timing windows that are relatively long, of the order of 10 nsec or greater.

A number of solutions have been proposed, including "staggered" partial septa to restrict the out-of-field-of-view component without greatly decreasing the axial acceptance angle for true coincidences, shielding the subject (rather than the detectors) by placing or wrapping some form of flexible lead over the part of the body outside the field of view, and decreasing the coincidence window width. As the random coincidence rate varies linearly with window width (recall $R_{ab} = 2\tau N_a N_b$ where 2τ is the width of the coincidence timing window), a decrease by a factor of two from 12 nsec to 6 nsec would be expected to halve the random event rate. However, this would be at the expense of energy and positioning information due to the need to truncate the pulses from the detectors. One simple solution that has been widely employed in brain studies is to add a removable lead shield to the end of the tomograph on the patient side, effectively extending the end shielding [34]. Unfortunately this is only applicable for brain studies. Nevertheless, it is very effective in this application [35].

The solution would appear to be to use a fast scintillator, such as LSO, YSO, or GSO, and a shorter coincidence window. However, a time window of 4 nsec or less would require the use of time-of-flight electronics as the time window duration is now approaching the time it would take for an annihilation photon produced at the edge of the transaxial field of view (perhaps from a transmission source) to travel to the opposing

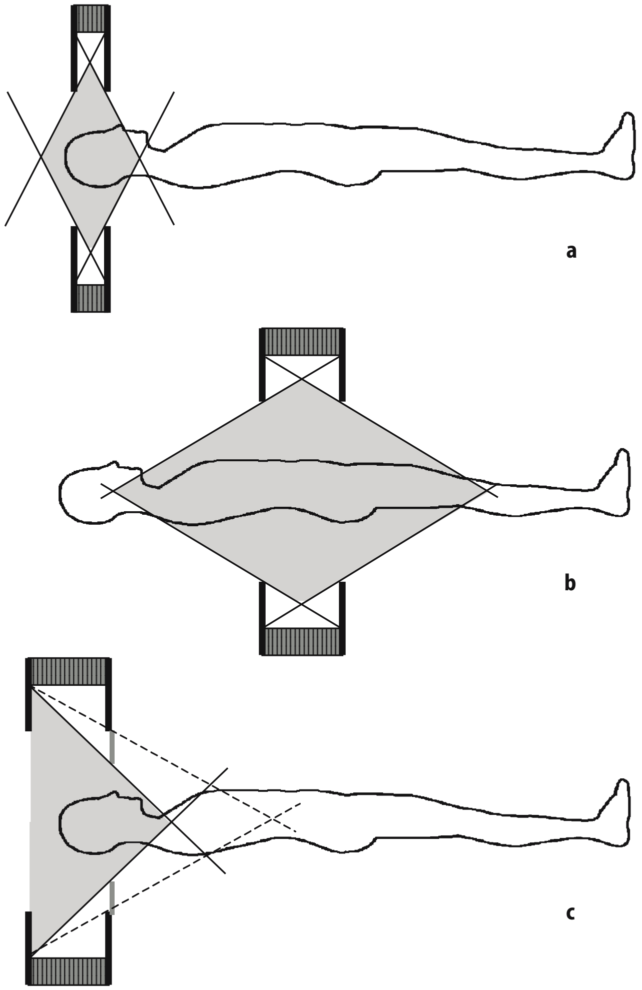

Figure 3.25. The field of view for single photons is shown schematically for three different scanner configurations in 3D. In (a), the first purpose-built 2D/3D tomograph (CTI ECAT 953B), which was designed for brain studies only, is shown. It had a 76 cm ring diameter, 10.8 cm axial field of view, and end shielding that restricted the subject aperture to 38 cm. In (b), the first purpose-built 3D-only full ring BGO tomograph (CTI EXACT3D) is shown. It had a 23.4 cm axial field of view and 82 cm ring diameter. However, as it was intended for whole-body scanning, the end shields were limited in extent to allow a large subject aperture (64 cm). This produced an enormous single-photon field of view which impacted on performance. A modification to the same tomograph, with removable lead end shields for use in brain studies (c), improved performance dramatically by restricting the single-photon field of view. The broken lines show the single-photon field of view without the shields in place.

detector, a distance close to one metre away. If non-time-of-flight electronics are employed the width of the transaxial field of view will be restricted.

There will also be an increase in true coincidences arising from outside the field of view in which one or both photons are scattered. This poses a problem for scatter-correction algorithms that use estimation methods, rather than direct measurements, to define the scatter contribution. Some algorithms combine both approaches by using the measured event rate outside the object being imaged, which must be due to scatter, to scale the estimated scatter within the object.

References

1. Derenzo SE, Zaklad H, Budinger TF. Analytical study of a high-resolution positron ring detector system for transaxial reconstruction tomography. J Nucl Med 1975;16(12):1166–73.
2. Derenzo SE. Method for optimizing side shielding in positron emission tomographs and for comparing detector materials. J Nucl Med 1980;21(10):971–7.
3. Kouris K, Spyrou NM, Jackson DF. Imaging with ionizing radiations. 1982 ed. Surrey: Surrey University Press; 1982.
4. Orlov S. Theory of three-dimensional reconstruction. 1. Conditions of a complete set of projections. Sov Phys Crystallogr 1976;20:312–4.
5. Defrise M, Townsend DW, Clack R. Three-dimensional image reconstruction from complete projections. Phys Med Biol 1989;34:573–87.
6. Kinahan PE, Rogers JG. Analytic 3-D image reconstruction using all detected events. IEEE Trans Nucl Sci 1989;NS-36:964–8.
7. Townsend DW, Spinks TJ, Jones T, Geissbühler A, Defrise M, Gilardi M-C, et al. Three-dimensional reconstruction of PET data from a multi-ring camera. IEEE Trans Nucl Sci 1989;36(1):1056–65.
8. Cherry SR, Dahlbom M, Hoffman EJ. 3D PET using a conventional multislice tomograph without septa. J Comput Assist Tomogr 1991;15:655–68.
9. Bailey DL, Jones T, Spinks TJ, Gilardi M-C, Townsend DW. Noise equivalent count measurements in a neuro-PET scanner with retractable septa. IEEE Trans Med Imag 1991;10(3):256–60.
10. Phelps ME, Hoffman EJ, Mullani NA, Ter-Pogossian MM. Application of annihilation coincidence detection to transaxial reconstruction tomography. J Nucl Med 1975;16(3):210–24.
11. Phelps ME, Hoffman EJ, Huang SC, Kuhl DE. ECAT: A new computerized tomographic imaging system for positron emitting radiopharmaceuticals. J Nucl Med 1978;19:635–47.
12. Hoffman EJ, Huang SC, Phelps ME. Quantitation in positron emission tomography: 1. Effect of object size. J Comput Assist Tomogr 1979;3(3):299–308.
13. Weber MJ, Monchamp RR. Luminescence of $Bi_4Ge_3O_{12}$: spectral and decay properties. J Appl Phys 1973;44:5495–9.
14. Cho Z, Farukhi M. Bismuth germanate as a potential scintillation detector in positron cameras. J Nucl Med 1977;18:840–4.
15. Casey ME, Nutt R. A multicrystal two-dimensional BGO detector system for positron emission tomography. IEEE Trans Nucl Sci 1986;NS-33(1):460–3.
16. Muehllehner G. Positron camera with extended counting rate capability. J Nucl Med 1975;16(7):653–7.
17. Muehllehner G, Karp JS, Mankoff DA, Beerbohm D, Ordonez CE. Design and performance of a new positron emission tomograph. IEEE Trans Nucl Sci 1988;35(1):670–4.
18. Karp JS, Muehllehner G, Geagan MJ, Freifelder R. Whole-body PET scanner using curve-plate NaI(Tl) detectors. J Nucl Med 1998;39:50P (abstract).
19. Karp JS, Muehllener G, Mankoff DA, Ordonez CE, Ollinger JM, Daube-Witherspoon ME, et al. Continuous-slice PENN-PET: a positron tomograph with volume imaging capability. J Nucl Med 1990;31:617–27.
20. Cranley K, Millar R, Bell T. Correction for deadtime losses in a gamma camera data analysis system. Eur J Nucl Med 1980;5:377–82.
21. Dainty JC, Shaw R. Image science: principles, analysis and evaluation of photographic-type imaging processes. London: Academic Press; 1974.
22. Wagner RF. Low-contrast sensitivity of radiologic, CT, nuclear medicine and ultrasound medical imaging systems. IEEE Trans Med Imag 1983;MI-2:105–21.

23. Strother SC, Casey ME, Hoffman EJ. Measuring PET scanner sensitivity: relating countrates to image signal-to-noise ratios using noise equivalent counts. IEEE Trans Nucl Sci 1990;37(2):783–8
24. NEMA. Performance measurements of positron emission tomographs. Washington: National Electrical Manufacturers Association; 1994. Report No. NU2-1994.
25. Bergström M, Eriksson L, Bohm C, Blomqvist G, Litton J-E. Correction for scattered radiation in a ring detector positron camera by integral transformation of the projections. J Comput Assist Tomogr 1983;7(1):42–50.
26. Burnham CA, Brownell GL. A multi-crystal positron camera. IEEE Trans Nucl Sci 1973;NS-19(3):201–5.
27. NEMA. Performance measurements of positron emission tomographs. Washington: National Electrical Manufacturers Association; 2001. Report No. NU2–2001.
28. Hoffman EJ, Phelps ME. Positron emission tomography: principles and quantitation. In: Phelps ME, Mazziotta JC, Schelbert HR, editors. Positron emission tomography and autoradiography. Principles and applications for the brain and heart. New York: Raven Press; 1986. pp. 237–86.
29. Phelps ME, Huang SC, Hoffman EJ, Plummer D, Carson RE. An analysis of signal amplification using small detectors in positron emission tomography. J Comput Assist Tomogr 1982;6(3):551–65.
30. Bailey DL, Jones T, Spinks TJ. A method for measuring the absolute sensitivity of positron emission tomographic scanners. Eur J Nucl Med 1991;18:374–9.
31. Bailey DL, Jones T. A method for calibrating three-dimensional positron emission tomography without scatter correction. Eur J Nucl Med 1997;24(6):660–4.
32. Bailey DL, Meikle SR, Jones T. Effective sensitivity in 3D PET: the impact of detector dead time on 3D system performance. IEEE Trans Nucl Sci 1997;NS–44:1180–5.
33. IEC. 61675-1: Radionuclide imaging devices – characteristics and test condition. Part I: Positron emission tomographs. Geneva: International Electrotechnical Commission; 1997. Report No. IEC 62C/205/FDIS.
34. Spinks TJ, Miller MP, Bailey DL, Bloomfield PM, Livieratos L, Jones T. The effect of activity outside the direct field of view in a 3D-only whole body positron tomograph. Phys Med Biol 1998;43(4):895–904.
35. Bailey DL, Miller MP, Spinks TJ, Bloomfield PM, Livieratos L, Bánáti RB, et al. Brain PET studies with a high-sensitivity fully 3D tomograph. In: Carson RE, Daube-Witherspoon ME, Herscovitch P, editors. Quantitative functional brain imaging using positron emission tomography. San Diego: Academic Press; 1998. pp. 25–31.